INORGANIC CHEMISTRY FRONTIERS

RESEARCH ARTICLE

View Article Online
View Journal | View Issue

Cite this: *Inorg. Chem. Front.*, 2022, **9**, 3828

Light induced ammonia synthesis by crystalline polyoxometalate-based hybrid frameworks coupled with the Sv-1T MoS_2 cocatalyst†

Fengrui Li,[a] Hongru Liu,[a] Weichao Chen, *[a,b] Ying Su,[a] Weilin Chen, *[a] Jingjing Zhi[a] and Yangguang Li *[a]

The exploration of efficient and stable composite-materials as nitrogen reduction photocatalysts featuring wide spectrum absorption and nitrogen fixation active sites has become specifically significant. In this work, a series of mixed-addendum PMoV-based organic–inorganic hybrid materials coupled with rich sulfur vacancy 1T MoS_2 (Sv-1T MoS_2) through a hydrothermal growth strategy are presented towards green NH_3 production. The intervalence electron transfer of the reduced polyoxometalates, as well as the construction of a Ni-trinuclear cluster-based framework, is responsible for the capable light-harvesting performance of the well-defined PMo_8V_6–Ni crystalline material, and Sv-1T MoS_2 which serves as a cocatalyst can facilitate electron–hole separation of the light absorbers, which further promotes the ammonia production capacity of the composite materials. As expected, the ammonia generation rate of Sv-1T MoS_2/PMo_8V_6–Ni (80.6 μmol h^{-1} g^{-1}) is much higher than that of either PMo_8V_6–Ni (9.7 μmol h^{-1} g^{-1}) or Sv-1T MoS_2 (8.6 μmol h^{-1} g^{-1}) component. Such a noble-metal-free system therefore shows an apparent quantum efficiency (AQE) of 0.368% at 550 nm. The "working-in-tandem" mechanism established by sulfur vacancies as nitrogen active sites and polyoxometalate crystalline photosensitizers are extremely crucial for facilitating N_2 chemisorption and NH_3 formation. This work provides a fresh perspective for the rational design of photocatalyst composite materials with energetic electrons towards efficient nitrogen fixation.

Received 8th May 2022,
Accepted 2nd June 2022

DOI: 10.1039/d2qi01003h

rsc.li/frontiers-inorganic

1. Introduction

Ammonia plays an irreplaceable role in the global chemical economy and agricultural development. At present, most of the ammonia manufacture worldwide still depends on the Haber–Bosch method that usually employs iron-based catalysts to fixate nitrogen with hydrogen under harsh reaction conditions.[1] The hydrogen in the reaction process was derived from steam-methane reforming, which discharges a large amount of carbon dioxide into the atmosphere.[2–4] With the rapid development of social civilization, seeking an efficient, sustainable, and green strategy is essential for the nitrogen reduction reaction (NRR).[5–8] The photocatalytic NRR operated under ambient pressure at room temperature in water possesses broad application prospects in view of its energy and environmental advantages.[9–16] A suitable NRR catalyst, the core of such a photocatalytic process, needs considerable visible-light absorption and enough active sites, whereas the state-of-the-art photocatalysts have always suffered from shortcomings, such as narrow range light absorption and high recombination of charge carriers.[17–19] The development of fire-new highly efficient and stable photocatalysts remains important for the conversion of N_2 into ammonia under mild conditions.

Inspired by the "working-in-tandem" mechanism of nitrogenase enzymes, the design and fabrication of bicomponent composite-materials might offer a promising photocatalyst family towards the nitrogen conversion.[20] This strategy is well-established in CdS/MoFe protein complexes.[21,22] In the CdS nanorod/MoFe protein biohybrid photocatalyst[9] reported by Wilker *et al.* in 2016, semiconductor nanocrystals served as a light absorber driving the enzyme (natural N_2 active sites) for effective NRR.[21] Similar composite-materials are widely used to explore the photocatalytic NRR performance, typical examples including Pt–SACs/CTF,[23] Ru/*n*-GaN nanowires,[24] Ru–K/B-*g*-C_3N_4,[25] *etc.* As expected, the synergistic effect of these photocatalytic NRR materials is originated from light absorber

[a]*Key Laboratory of Polyoxometalate and Reticular Material Chemistry of Ministry of Education, Department of Chemistry, Northeast Normal University, Ren Min Street No. 5268, Changchun, Jilin, 130024, P. R. China. E-mail: chenwl@nenu.edu.cn, liyg658@nenu.edu.cn*

[b]*Key Laboratory of Preparation and Application of Environmental Friendly Materials, Jilin Normal University, Ministry of Education, Changchun, 130103, China*

†Electronic supplementary information (ESI) available. CCDC 2096404, 2120049 and 2120050. For ESI and crystallographic data in CIF or other electronic format see DOI: https://doi.org/10.1039/d2qi01003h

species as well as cocatalysts (*e.g.* expensive enzymes and noble metals) featuring nitrogen fixation active sites. There is no doubt that the large-scale applications of such cocatalysts are severely impeded by the high costs and rare resources.[26,27] Fortunately, Sv-1T MoS_2 materials as ideal non-noble metal cocatalysts could be designed for NRR photocatalysis. Its sulfur vacancies may not only engineer the band or electronic structure of the overall catalyst, but also bring superior impacts on the photocatalytic NRR process through offering extra sites for nitrogen fixation activation and adsorption[28] as confirmed by density functional theory.[29] To our knowledge, the current NRR catalysts based on Sv-1T MoS_2 cocatalysts are mainly focused on the electrocatalysis model.[30–32] The exploration of more efficient and stable composite NRR photocatalysts based on Sv-1T MoS_2 cocatalysts will be a significant topic.

Polyoxometalates (POMs), a critical class of metal–oxygen clusters, can act as promising candidates for the efficient utilization of light to combine with Sv-1T MoS_2 cocatalysts, because: (1) the elementary composition and electronic structures of POMs can be modulated at the molecular level. Their oxygen-rich surface can be easily activated and modified, which is beneficial for preparing accessible POM-based composite-materials. (2) Reduced POMs (also called heteropoly blues, a reductive state of POMs) are famous for wide and strong spectral absorptions in the UV-visible region and sometimes in the near-IR region on account of their intervalence-charge transfer, indicating a new type of light absorber species that can drive the nitrogen fixation process. (3) POMs possess a nanometer size, robust redox stability, and excellent thermal and acid–base stability.[33] The cheap raw materials, and green and simple synthesis method endow POMs with broad application prospects. In this stage, the reduced PMoV system displays a wide photoabsorption spectrum, thanks to the incorporation of low-valance Mo or V elements (Mo^{5+}/V^{4+}) featuring *d–d* transfer.[34] Such light absorption can be further broadened through building POM-metal–organic hybrid architectures so as to satisfy the energy provision of NRR. Herein, three organic–inorganic hybrid materials based on the Keggin PMoV cluster and classical Ni-trinuclear metal organic skeletons have been obtained, from the $[H_2bpy]_2[H_3PMo_8^{VI}V_6^{IV}O_{42}]\cdot 6H_2O$ (bpy = 4,4′-bipyridine) (PMo_8V_6) cluster to the $[Ni_7(trz)_{12}(H_2O)_8][PMo_8^{VI}Mo_3^{V}V_{3.5}^{IV}O_{42}]\cdot 12H_2O$ ($PMo_{11}V_{3.5}$–Ni) and $[Ni_7(trz)_{12}(H_2O)_8][HPMo_8^{VI}V_4^{V}V_2^{IV}O_{42}]\cdot 17H_2O$ (trz = 1,2,4-triazole) (PMo_8V_6–Ni) frameworks. The reduced Mo–V centers with different element composition proportions as well as photoactive Ni-trinuclear cluster-based frameworks give rise to different light absorption performances of such structures. Consequently, a combination of Sv-1T MoS_2 and PMoV-based hybrid materials under a hydrothermal growth strategy is expected to be efficient nitrogen reduction photocatalysts (Scheme 1). It is demonstrated that Sv-1T MoS_2/PMo_8V_6–Ni displays the best photocatalytic N_2 activity with the optimal NH_3 generation rate of 80.6 μmol h^{-1} g^{-1}, which holds an AQE of 0.368% at 550 nm.

2. Results and discussion

2.1. Crystal structures of PMoV-based hybrid frameworks

The formation conditions of the three compounds are shown in Fig. 1. PMo_8V_6 remains an isolated cluster while $PMo_{11}V_{3.5}$–Ni and PMo_8V_6–Ni are isomorphous POM-based organic–in-

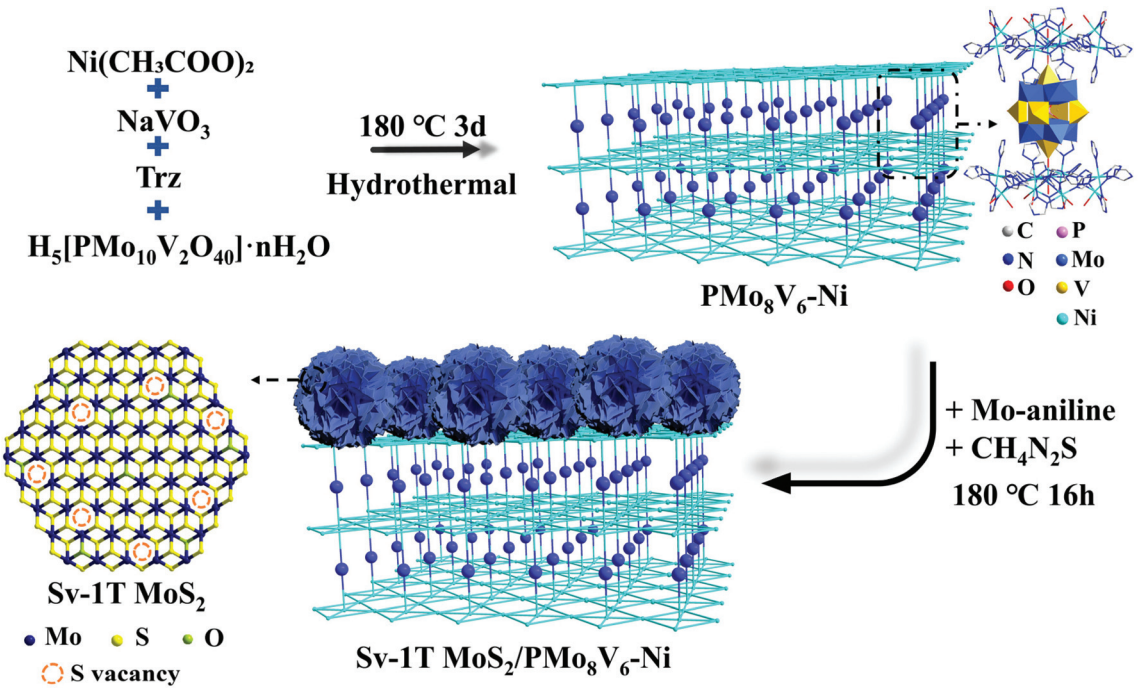

Scheme 1 Illustration of the Sv-1T MoS_2/PMo_8V_6–Ni preparation process.

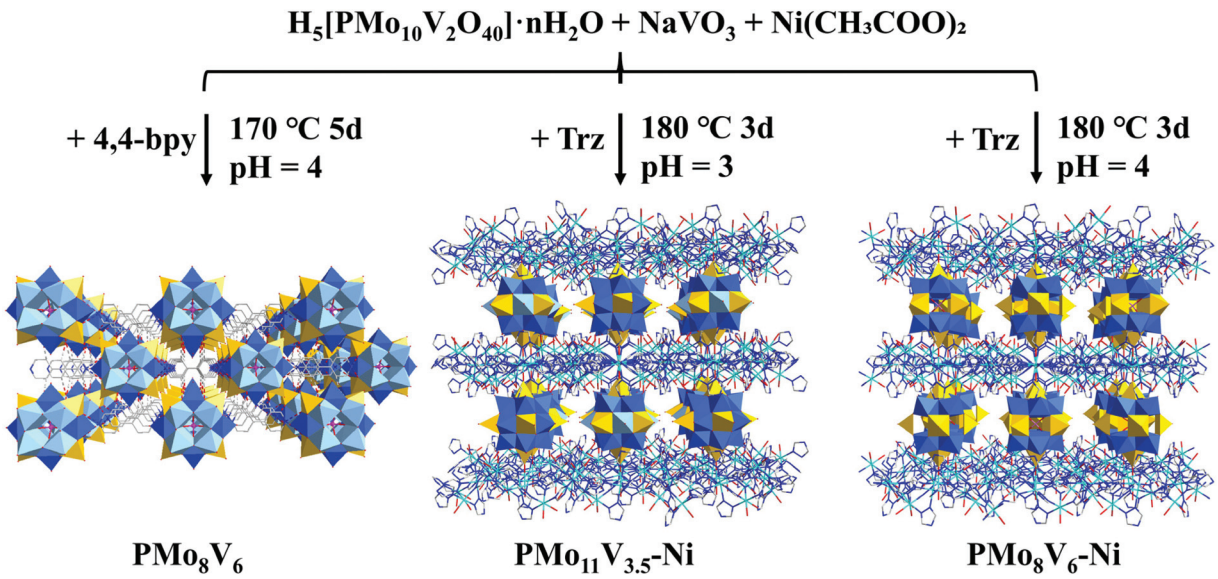

Fig. 1 Illustration of the PMoV-based hybrid materials preparation process (color code: C gray, N drak blue, O red, P pink, Mo blue, V yellow, Ni indigo, Mo/V light blue).

organic hybrid frameworks. X-ray crystallography diffraction showed that the main difference in both frameworks is derived from the Mo/V molar ratios in similar Keggin PMo_mV_n clusters (m = 11 and n = 3.5 for $PMo_{11}V_{3.5}$–Ni, m = 8 and n = 6 for PMo_8V_6–Ni, respectively). In practical terms, PMo_8V_6–Ni consists of two $[PMo_8V_4O_{40}(VO)_2]^{3-}$ units, three Ni atoms, three deprotonated Trz ligands, and eight water molecules (Fig. S1†). The classical Keggin PMoV clusters capped by two crystallographically independent V^{4+} cations (V1 and V2, Fig. S2†) at the two "pit positions" of opposite $\{Mo_4O_{18}\}$ tetramers give rise to the final $[PMo_8V_4O_{40}(VO)_2]$ units. Interestingly, such units had also been isolated with the cocrystallization of bpy ligands in PMo_8V_6 (Fig. S3†). Moreover, three crystallographically independent nickel atoms with hexacoordination geometries in PMo_8V_6–Ni exhibit different coordination environments. The Ni1 atom (Fig. S2†) linked one N atom on the Trz ligand and two O atoms from two opposite V cap centers. Ni2 and Ni3 atoms (Fig. S2†) were coordinated with six Trz ligands and four water molecules to form classical linear metal trinuclear clusters as reported by Lan *et al.*[35] In all, the formations of unexampled Keggin PMo_mV_n clusters and Ni-Trz linkers are important for the assemblies of these compounds. All three POM-based hybrids, from the isolated cluster to cluster-based frameworks, exhibit attainable photochemical activities in terms of the intervalence-charge transfer in the reduced PMo_mV_n units and its integrations with photoactive Ni-trinuclear clusters.

2.2. Morphology and characterization of composite-materials

The as-prepared PMoV-based hybrids and Sv-1T MoS_2 formed *in situ* were combined successfully through a hydrothermal growth strategy. The morphology and microstructures of Sv-1T MoS_2 and Sv-1T MoS_2/PMoV-based hybrid composite-materials were explored using SEM and TEM. The morphology of Sv-1T MoS_2 presents flower-like morphologies as shown in Fig. 2a and such a structure is further confirmed by TEM analysis (Fig. 2c). After integrating with the PMoV-based hybrid materials, the flower-like morphologies of Sv-1T MoS_2 had been maintained (Fig. 2b and d). The high-resolution TEM (HRTEM) image of composite-materials, as displayed in Fig. 2e, provides information about the interface between Sv-1T MoS_2 and PMoV-based hybrid materials, which showed that Sv-1T MoS_2 nanoflowers were closely attached to the PMoV-based hybrid materials, and such combination may boost the charge transfer efficiency. In detail, the lattices with d spacing of 0.70 and 0.27 nm are attributed to the (002) and (100) planes of 1T MoS_2, which are equal to those in the literature.[36,37] The S vacancies in the structure of the composite-materials were observed, typically consisting of cracks and misaligned basal planes (Fig. 2f and S4†). The energy dispersive X-ray (EDX) result and elemental mappings show that Mo, S, V, Ni, and O are uniformly distributed on the composite-materials (Fig. 2g and S5†).

The FTIR spectra of Sv-1T MoS_2, PMoV-based hybrid materials, and Sv-1T MoS_2/PMoV-based hybrid composite-materials are shown in Fig. 3a and S6.† The maintenance of classical POM stretching vibration in PMoV-based hybrid materials at 750–1600 cm^{-1} verifies the combination of Sv-1T MoS_2 and PMo_8V_6–Ni. In this connection, the peak positions display a slight shift, which may be caused by the interaction between Sv-1T MoS_2 and PMoV-based hybrid materials.[38] The XRD patterns of 1T MoS_2 and Sv-1T MoS_2 display two characteristic diffractions of (002) and (004) that are moved to 9.0 and 18.5°, which manifest the existence of the 1T phase (Fig. 3b and S7†).[39] Similarly, the change of peak intensity indicates the difference in crystallinity, which shows that

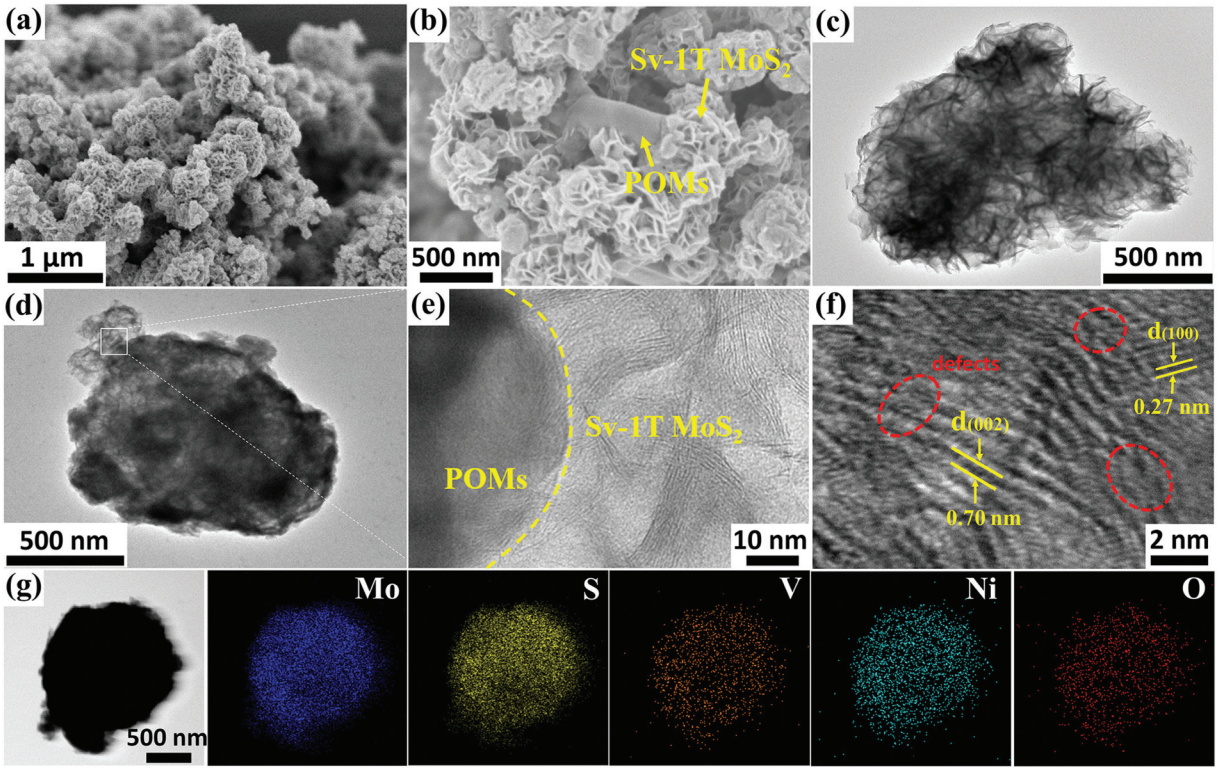

Fig. 2 (a) SEM and (c) TEM images of Sv-1T MoS_2; (b) SEM, (d) TEM, and (e), (f) HRTEM of the Sv-1T MoS_2/PMo_8V_6–Ni composite-material; (g) EDX mapping of Mo, S, V, Ni, and O in the Sv-1T MoS_2/PMo_8V_6–Ni composite-material.

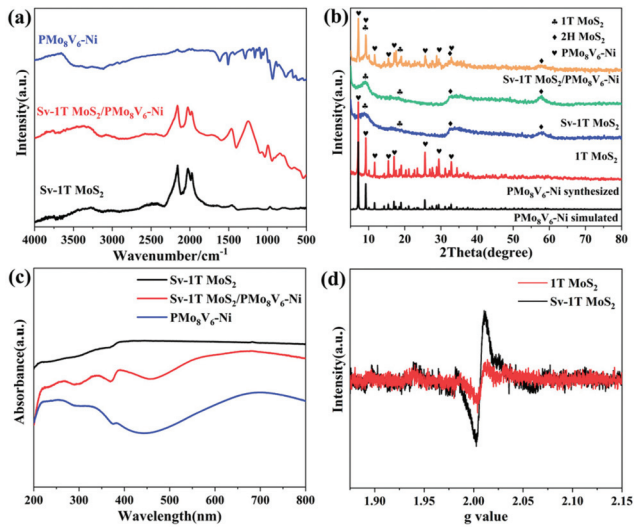

Fig. 3 (a) FT-IR spectra, (b) XRD patterns, and (c) UV-vis diffuse reflectance spectra of Sv-1T MoS_2, PMo_8V_6–Ni, and Sv-1T MoS_2/PMo_8V_6–Ni composite-materials, and (d) EPR spectra of 1T MoS_2 and Sv-1T MoS_2.

sulfur vacancy treatment boosts 1T MoS_2 crystallinity. By comparing the experimental and simulated diffraction peaks, the XRD analysis of PMoV-based hybrid materials matches the key peak positions, which manifests the phase purity of hybrid materials. As for the composite-materials, the observed characteristic peaks of Sv-1T MoS_2 and PMoV-based hybrid materials suggest that both components exist simultaneously in the composite-materials. Thermogravimetric analysis (TG) manifested that three PMoV-based hybrid materials possess suitable thermostability (below 250 °C) for combination with Sv-1T MoS_2 under hydrothermal conditions (Fig. S8†). The UV-vis diffuse spectra were recorded in order to validate the visible-light-enrichment capability. As shown in Fig. 3c, it can be precisely observed that Sv-1T MoS_2 possesses a flat plot with a high absorption coefficient over the UV-vis region, indicating that Sv-1T MoS_2 displays a metallic character.[37,39,40] The absorption spectra of PMoV-based hybrid materials are shown in Fig. S9.† PMo_8V_6–Ni possesses better absorption intensity than $PMo_{11}V_{3.5}$–Ni at 500–800 nm, which may result from the intervalence-electronic transition or metal-to-metal charge transfer from the low-valance V to high-valance Mo or V centers, respectively.[34,41] The introduction of the metal cluster as bridging units endows PMo_8V_6–Ni and $PMo_{11}V_{3.5}$–Ni 3D polymers with better light absorption than that of the isolated PMo_8V_6 cluster (Fig. S10†). Thanks to the combination of mixed-addendum PMoV building blocks and framework architecture construction; PMo_8V_6–Ni exhibits outstanding light absorption capacity. Overall, Sv-1T MoS_2/PMoV-based hybrid composite-materials have a wide absorption range so as to enhance the utilization of light, which holds a great advantage for driving NRR in the form of light as the energy source. The electron paramagnetic resonance (EPR) spectrum was verified

to estimate the concentration of S vacancies.[29,42,43] The S vacancies can provide unsaturated sites for facilitating the generation of a great number of unpaired electrons (Fig. 3d). The intensity of the EPR signal is proportional to the concentration of dangling bonds from the S vacancies in MoS_2. The high EPR signal corresponds to a high concentration of S vacancies in Sv-1T MoS_2, which proves that Sv-1T MoS_2 possesses more S vacancies than 1T MoS_2.

The chemical environment and valence states of the as-prepared samples were further analyzed *via* X-ray photoelectron spectroscopy (XPS) measurements. The Mo 3d spectrum of 1T MoS_2 is shown in Fig. 4a, and the four peaks around 228.2/231.4 eV and 229.4/232.6 eV are ascribed to the 1T phase and 2H phase of Mo^{IV} $3d_{5/2}$ and Mo^{IV} $3d_{3/2}$, respectively,[37,44] which are consistent with the XRD results. The peaks at 225.6 eV and 235 eV came from the typical S 2s and Mo–O bonds, respectively. The four peaks in the S 2p spectrum around 161.1/162.1 eV and 162.5/163.7 eV are ascribed to the peaks of the 1T phase and 2H phase of S $2p_{3/2}$ and S $2p_{1/2}$, respectively (Fig. 4b). A S–O peak is located at 168.6 eV. The characteristic peaks of Sv-1T MoS_2 are slightly shifted to high binding energies and their intensity is weaker than that of 1T MoS_2 due to the impact of sulfur vacancies on the crystallization degree.[45,46] The Mo–O bond signals in the Mo 3d spectrum and S–O bond signals in the S 2p spectrum confirm the incorporation of O. The results further verify the existence of sulfur vacancies and O-doped. Furthermore, Fig. 4c shows the S 2p peaks of all three composite-materials; obvious peak shifts could be observed when compared to S 2p peaks in Sv-1T MoS_2, which clearly indicates that both PMoV-based hybrids and Sv-1T MoS_2 are combined effectively with essential charge transfer at their interfaces rather than simple physical mixing.[47,48] The Mo 2p, Ni 2p, and V 2p spectra of the composite-materials are also observed which may be arisen from the reduction process of PMoV-based hybrids in the presence of thiourea.[49] The binding energies at 232.9 and 235.7 eV imply the Mo^{VI} centers (Fig. 4d). The characteristic peaks of nickel can be apparently observed, which are centered at 874.5 eV of Ni $2p_{1/2}$ and 856.1 eV of Ni $2p_{3/2}$, and the corresponding satellite peaks (879.8 and 861.6 eV) are also observed in the Ni 2p spectra (Fig. 4e and S11†).[48] The high resolution V 2p XPS spectrum features four peaks at 524.6/517.7 eV and 523.7/516.3 eV, which are assigned to V^{V} and V^{IV} (Fig. 4f and S12†).[50] In total, all XPS spectra further offer strong evidence for the successful combination of POMs and Sv-1T MoS_2.

2.3. Photocatalytic nitrogen fixation studies

The design of the Sv-1T MoS_2/PMoV-based hybrid composite-materials possessing wide range light absorption allows for the exploration of its photocatalytic NRR activity under illumination (Fig. 5a and S13†). The photocatalytic NRR activity of Sv-1T MoS_2 is higher than that of 1T MoS_2, thanks to the existence of S vacancies (Fig. S14a†). The NRR activity of the Sv-1T MoS_2/PMo_8V_6 hybrid materials with different Sv-1T MoS_2 amounts was evaluated (Fig. S13b†). The NRR activity

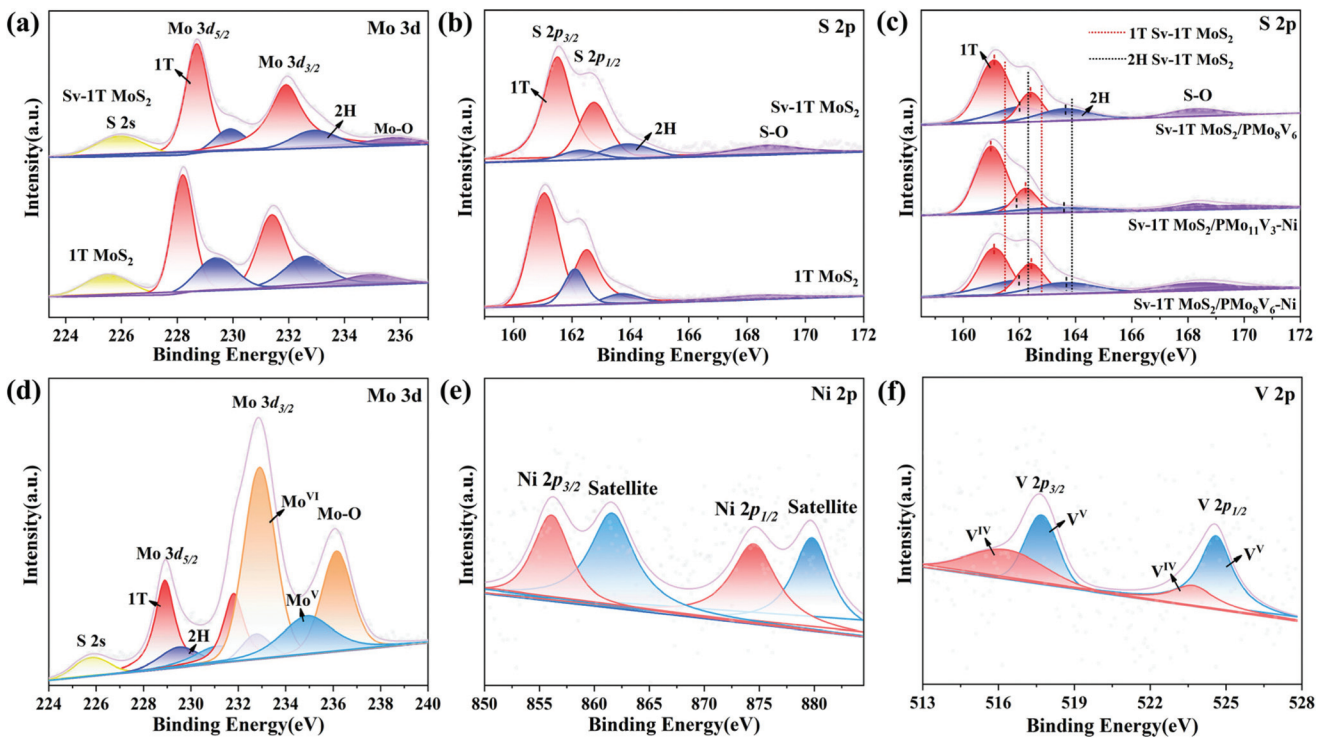

Fig. 4 XPS spectra of (a) Mo 3d and (b) S 2p for Sv-1T MoS_2 and 1T MoS_2. (c) S 2p spectra of Sv-1T MoS_2/PMoV-based hybrid composite-materials. (d) Mo 3d, (e) Ni 2p, and (f) V 2p spectra of Sv-1T MoS_2/PMo_8V_6–Ni hybrid composite-materials.

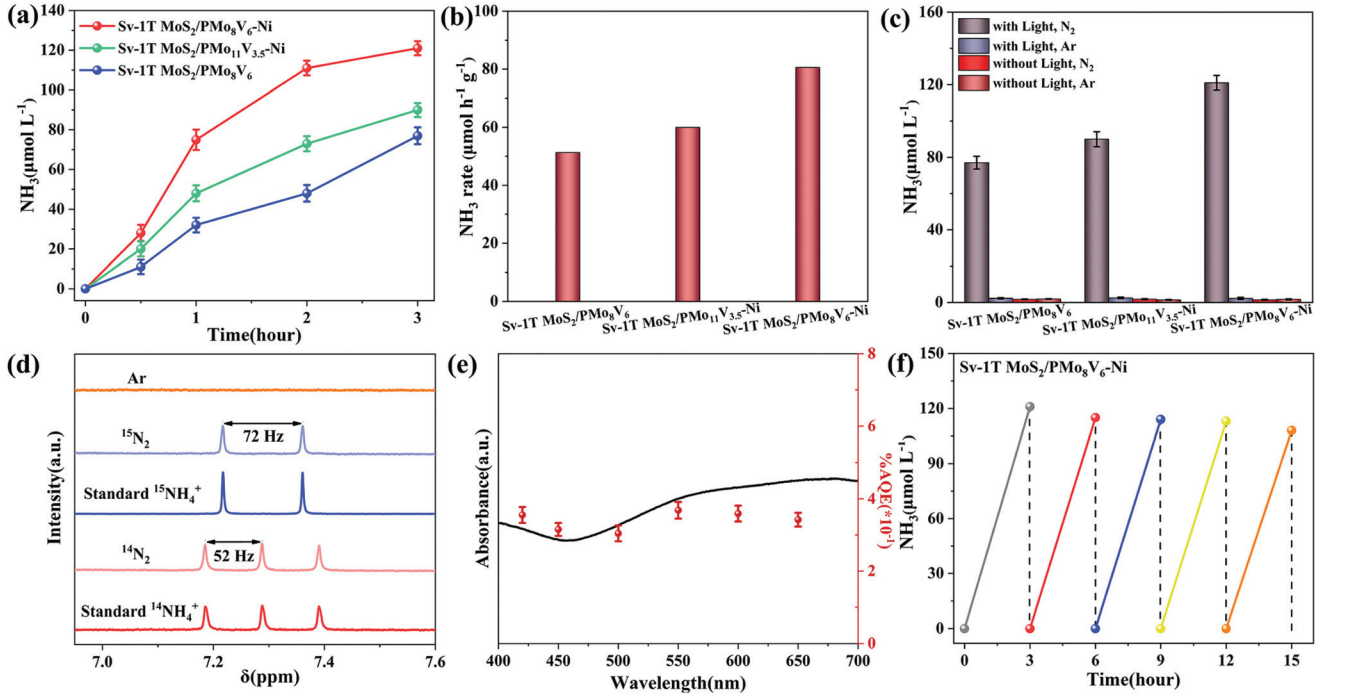

Fig. 5 (a) Ammonia production and (b) ammonia production rate of Sv-1T MoS_2/PMoV-based hybrid composite-materials. (c) Catalytic performance of Sv-1T MoS_2/PMoV-based hybrid composite-materials under a N_2 or Ar atmosphere. (d) ^{1}H-NMR spectra of Sv-1T MoS_2/PMo_8V_6–Ni. (e) Wavelength-dependent AQE for N_2 photofixation with Sv-1T MoS_2/PMo_8V_6–Ni under monochromatic light irradiation. (f) Cyclic stability of Sv-1T MoS_2/PMo_8V_6–Ni after five test cycles.

increases with the Sv-1T MoS_2 amount, reaches the highest value of 77 μmol L^{-1} with the Sv-1T MoS_2 amount of 40 wt%, and then decreases probably due to the masking effect of MoS_2,[51,52] which displays a nearly volcano-shaped reliance on the Sv-1T MoS_2 amount. As a consequence, we select this ratio as the best one for further study. The ammonia generation rate of Sv-1T MoS_2/PMo_8V_6–Ni (80.6 μmol h^{-1} g^{-1}) is higher than that of either the PMo_8V_6–Ni (9.7 μmol h^{-1} g^{-1}) or the Sv-1T MoS_2 (8.6 μmol h^{-1} g^{-1}) component, indicating that the S vacancies of Sv-1T MoS_2 as the adsorbed and activated nitrogen sites combined with PMoV-based hybrid materials as photogenerated electron donors play key roles in the photocatalytic NRR. Under similar catalytic conditions, such hybrid composite-materials can be comparable to Wang's Au/TiO_2–OV[2] with 78.6 μmol h^{-1} g^{-1}, Zhang's Au/end-CeO_2 [53] with 114 μmol h^{-1} g^{-1}, Xiong's AuRu core-antenna[54] with 101.4 μmol h^{-1} g^{-1}, *etc*. Moreover, Sv-1T MoS_2/PMo_8V_6–Ni possesses a more superior ammonia production rate than the other Sv-1T MoS_2/PMoV-based hybrid composites, manifesting that the Mo/V ratio variation of PMoV building blocks and the introduction of hybrid frameworks into the PMoV-based hybrid materials can affect the photocatalytic NRR activity (Fig. 5a and b, and S14†). The ammonia signal was not detected in the absence of any one of the following: the nitrogen source, pure water as proton sources, and illumination, which are essential for the photocatalytic NRR (Fig. 5c and S15†). The parallel experiments indicated that the O_2 product is not detected after using ethanol as the hole sacrificial agent (Fig. S16 and S17†), indicating that the holes are consumed by the sacrificial agent and no N_2H_4 is detected as a byproduct of the photocatalytic NRR.

The various sources of contamination (for example, nitrates, nitrites and nitrogen oxides) will affect the final ammonia content. The rigorous protocols can ensure the nitrogen source of ammonia.[6] According to Andersen's purification method,[6] the feeding gases (high-purity Ar (99.999%), $^{14}N_2$ (99.999%) and $^{15}N_2$ (99 atom%)) were carefully purified to further verify the origin of the ammonia generated from NRR. The isotope labeling experiments were executed using the purified feeding gas as the nitrogen sources, which was confirmed *via* the ^{1}H-NMR spectrum. The triplet and doublet peaks related to $^{14}NH_4^+$ and $^{15}NH_4^+$ can be clearly emerged in the ^{1}H-NMR spectrum, respectively. The coupling constants are J_{N-H} = 52 Hz and J_{N-H} = 72 Hz, which reaffirms that the produced NH_3 indeed originates from NRR (Fig. 5d). To appraise the light utilization efficiency, the wavelength-dependent apparent quantum efficiencies (AQEs) of Sv-1T MoS_2/PMo_8V_6–Ni were evaluated by calculating at various wavelengths of monochromatic light irradiation (Fig. 5e). The AQE spectrum of Sv-1T MoS_2/PMo_8V_6–Ni matches its absorption spectrum, suggesting that the ammonia synthesis is driven by light. The AQE value of Sv-1T MoS_2/PMo_8V_6–Ni reaches 0.368% at 550 nm, thanks to the synergistic effect of the nitrogen activation and light harvesting, which can be comparable to that of classical materials reported recently, for example, Fe–TiO_2/Au (0.39% at 600 nm),[55] Mo–$W_{18}O_{49}$ (0.33% at 400 nm)[56] and

amorphous SmOCl nanosheets (0.32% at 420 nm)[57] (Table S1†). Sv-1T MoS_2/PMo_8V_6–Ni achieves a solar-to-ammonia conversion efficiency value of 0.024% under simulated AM 1.5G irradiation (Table S2†). The NRR activity remains nearly unchanged after five runs of the photocatalytic test, suggesting that the Sv-1T MoS_2/PMoV-based hybrid composite-materials possess good stability for the photo-driven NRR (Fig. 5f and S18†). The sample characterization studies (IR, XRD, SEM and XPS) after cycling tests do not undergo obvious change in comparison with the fresh ones, indicating the good reusability and stability of Sv-1T MoS_2/PMoV-based hybrid composite-materials for photocatalytic nitrogen reduction (Fig. S19 and S20†).

2.4. Mechanism studies of nitrogen reduced reaction

Effective charge separation and transfer is an indispensable process for activating nitrogen. To verify the separation and transfer of electron–hole pairs, photoelectrochemical characterization studies were performed including steady photoluminescence (PL), time-resolved PL spectroscopy, electrochemical impedance spectra (EIS), and photocurrent responses. The separation and migration of photogenerated electron–hole pairs can be demonstrated by steady PL. The PMoV-based hybrid materials have obvious absorption peaks at about 425–550 nm because of the quick recombination of electrons–hole pairs. After the combination of Sv-1T MoS_2, the Sv-1T MoS_2/PMoV-based hybrid composite-materials exhibit rapid fluorescence quenching, and the intensity of the corresponding fluorescence absorption peak becomes weaker (Fig. 6a and S21†). The electron–hole separation in the PMoV-based hybrid materials is accelerated through injecting electrons into Sv-1T MoS_2 as an electron acceptor. The time-resolved PL spectra indicated that the average radiative lifetimes (τ_{av}) of PMo_8V_6, $PMo_{11}V_{3.5}$–Ni, PMo_8V_6–Ni, Sv-1T MoS_2/PMo_8V_6, Sv-1T MoS_2/$PMo_{11}V_{3.5}$–Ni, and Sv-1T MoS_2/PMo_8V_6–Ni are 0.3297, 0.4095, 0.3711, 0.3029, 0.3456, and 0.2553 ns, respectively, which indicated the presence of more efficient nonradiative decay pathways in the Sv-1T MoS_2/PMoV-based hybrid composite-materials than in the PMoV-based hybrid materials (Fig. 6b and S22†). The photogenerated electron transfer efficiency can be characterized *via* the photocurrent responses measured in air and nitrogen, respectively (Fig. 6c and S23†). Sv-1T MoS_2/PMo_8V_6–Ni had a stable and stronger photocurrent than PMo_8V_6–Ni, which reflected the higher separating and transfer efficiency of photoexcited electron–hole pairs in Sv-1T MoS_2/PMo_8V_6–Ni. Undoubtedly, Sv-1T MoS_2/PMo_8V_6–Ni is beneficial for producing more photoexcited carriers for the photocatalytic NRR. The current intensity of the same under nitrogen is marginally smaller than that in air, indicating the existence of a certain degree of photogenerated electron consumption to dissociate the N≡N triple bond. The EIS Nyquist change was in agreement with the photocurrent results. Sv-1T MoS_2/PMo_8V_6–Ni possesses a smaller arc than PMo_8V_6, indicating that Sv-1T MoS_2/PMo_8V_6–Ni displayed the lowest charge-transfer resistance (Fig. 6d). Given the above discussions, the coupling of the S vacancy 1T MoS_2 with the PMoV-based hybrid materials could enhance the charge separation and transfer, further boosting the photocatalytic performance.

Mott–Schottky curves were verified to study the conduction band potential (E_{CB}) of materials. All the samples have positive slopes of the plots, revealing that they were n-type materials. The flat band potential (E_{FB}) of PMo_8V_6–Ni is −0.54 V *versus* NHE (Fig. S24†). The corresponding E_{CB} could be approximated to be −0.44 V *versus* NHE. The bandgap energy (E_g) values of PMo_8V_6, $PMo_{11}V_{3.5}$–Ni, and PMo_8V_6–Ni were verified using an UV-vis spectrometer (Fig. S25†). The VB potential (E_{VB}) can be obtained using $E_{VB} = E_g + E_{CB}$; the E_{VB} of PMo_8V_6–Ni is calculated as 2.32 V. On the basis of the XPS spectrum of the valence band of Sv-1T MoS_2, the position is approximately 0 eV, demonstrating that Sv-1T MoS_2 appertains to the metal phase (Fig. S26†).[44,47,58] From the above results, PMo_8V_6–Ni possesses a more negative potential than other hybrid materials, resulting in a sufficient potential difference between PMo_8V_6–Ni and Sv-1T MoS_2 for facilitating the electron transport. This bandgap range is fully compliant with the energy requirements of the photocatalytic NRR. When PMo_8V_6–Ni hybrid materials and Sv-1T MoS_2 are excited by illumination, the electrons on the Lowest Unoccupied Molecular Orbital (LUMO) level of PMo_8V_6–Ni hybrid materials transfer to the Sv-1T MoS_2 cocatalyst for the photocatalytic NRR. Based on the above experiments, we concluded that the photocatalytic NRR of the Sv-1T MoS_2/PMo_8V_6–Ni hybrid composite-material can be mainly split into three steps (Scheme 2): (1) the nitrogen fixation active sites of Sv-1T MoS_2/PMo_8V_6–Ni are largely exposed, so that N_2 is adsorbed on the S vacancies. (2) The photoexcited electrons from the PMoV-based hybrid materials transfer into the adsorbed nitrogen and convert it to the activated N_2 under illumination. (3) The holes of PMoV-based hybrid materials are consumed by the sacrificial agent; meanwhile, the protons and photoexcited electrons combined with the activated N_2 generate ammonia.

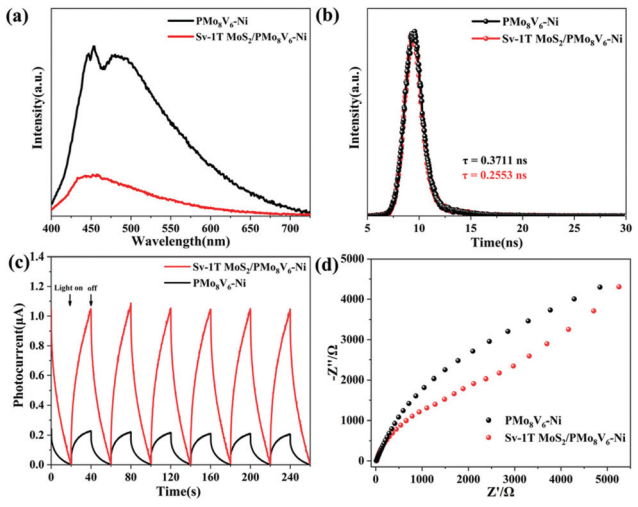

Fig. 6 (a) Steady PL spectra, (b) time-resolved PL spectra, (c) photocurrent responses, and (d) EIS Nyquist plots of PMo_8V_6–Ni and Sv-1T MoS_2/PMo_8V_6–Ni.

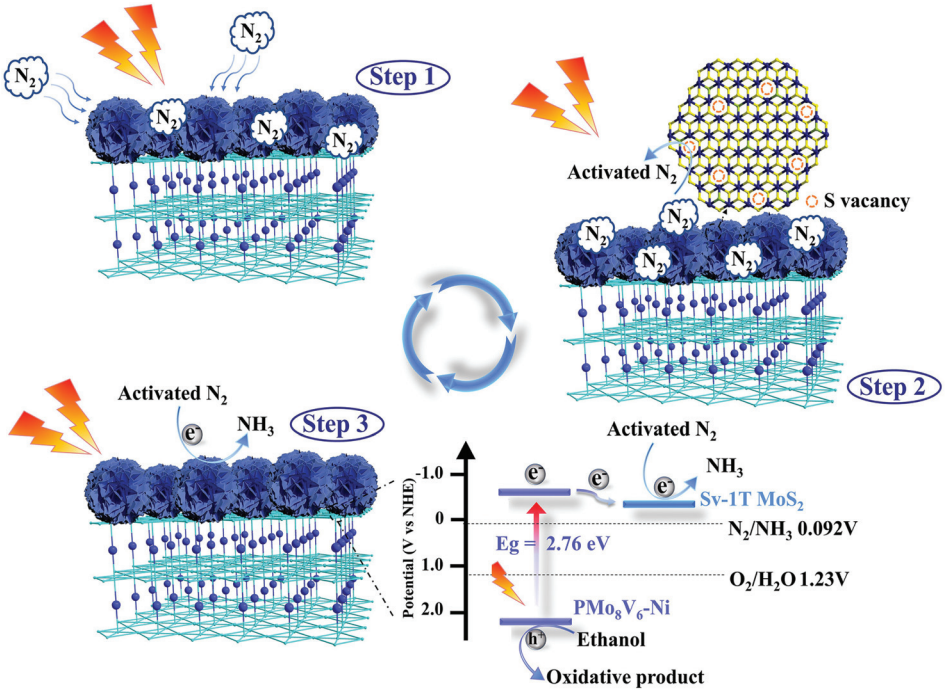

Scheme 2 Schematic illustration of the proposed mechanism for photocatalytic nitrogen fixation.

3. Conclusions

In summary, a series of mixed-addendum PMoV-based organic–inorganic hybrid materials as light absorbers were designed and prepared to fabricate Sv-1T MoS_2/PMoV-based hybrid composite-materials *via* a hydrothermal growth strategy, in which the S vacancies of Sv-1T MoS_2 act as activation sites and PMoV-based hybrid materials play the part of the light driving force for NRR. Sv-1T MoS_2/PMo_8V_6–Ni (80.6 μmol h^{-1} g^{-1}) possesses wide range light absorption and exhibits higher photocatalytic NRR efficiency than other Sv-1T MoS_2/PMoV-based hybrid composite-materials. The construction of composite-materials can boost the charge separation and transfer efficiency of the photoexcited electron–holes of photocatalysts, which distinctly enhances the performance of the photocatalytic NRR. It's worth noting that PMoV-based hybrid materials have been first introduced into the field of photocatalytic NRR, which provides wide range light absorption for the design of photo-driven NRR materials. Future work will involve the design of other types of POM-based hybrid materials and exploration of their photocatalytic NRR applications.

4. Experimental

The materials preparation, characterization, and NRR photochemical measurement of the as-prepared samples are described in detail in the Experimental section of the ESI.†

Conflicts of interest

There are no conflicts to declare.

Acknowledgements

This work was financially supported by the Natural Science Foundation of Jilin Province – Free Exploration General Project (YDZJ202201ZYTS331), NSFC of China (no. 21801038), the Science and Technology Research Foundation of Jilin Educational Committee (JJKH20221158KJ), the Open Project Program of Key Laboratory of Preparation and Application of Environmental Friendly Materials (Jilin Normal University), Ministry of Education, China (No. 2021004).

Notes and references

1 B. M. Hoffman, D. Lukoyanov, Z. Y. Yang, D. R. Dean and L. C. Seefeldt, Mechanism of Nitrogen Fixation by Nitrogenase: The Next Stage, *Chem. Rev.*, 2014, **114**, 4041–4062.

2 J. H. Yang, Y. Z. Guo, R. B. Jiang, F. Qin, H. Zhang, W. Z. Lu and J. F. Wang, High-efficiency "Working-in-Tandem" Nitrogen Photofixation Achieved by Assembling Plasmonic Gold Nanocrystals on Ultrathin Titania Nanosheets, *J. Am. Chem. Soc.*, 2018, **140**, 8497–8508.

3 C. Lv, Y. Qian, C. Yan, Y. Ding, Y. Liu, G. Chen and G. Yu, Defect Engineering Metal-free Polymeric Carbon Nitride

Electrocatalyst for Effective Nitrogen Fixation under Ambient Conditions, *Angew. Chem., Int. Ed.*, 2018, **57**, 10246–10250.

4 P. S. Li, Z. Zhou, Q. Wang, M. Guo, S. W. Chen, W. Liu, Y. Y. Wu and Y. J. Xiong, Visible-light-driven Nitrogen Fixation Catalyzed by Bi5O7Br Nanostructures: Enhanced Performance by Oxygen Vacancies, *J. Am. Chem. Soc.*, 2020, **142**, 12430–12439.

5 G. Marnellos and M. Stoukides, Ammonia Synthesis at Atmospheric Pressure, *Science*, 1998, **282**, 98–100.

6 S. Z. Andersen, V. Čolić, S. Yang, J. A. Schwalbe, A. C. Nielander, J. M. McEnaney, K. Enemark-Rasmussen, J. G. Baker, A. R. Singh, B. A. Rohr, M. J. Statt, S. J. Blair, S. Mezzavilla, J. Kibsgaard, P. C. K. Vesborg, M. Cargnello, S. F. Bent, T. F. Jaramillo, I. E. L. Stephens, J. K. Nørskov and I. Chorkendorff, A Rigorous Electrochemical Ammonia Synthesis Protocol with Quantitative Isotope Measurements, *Nature*, 2019, **570**, 504–508.

7 H. C. Tao, C. Choi, L. X. Ding, Z. Jiang, Z. S. Han, M. W. Jia, Q. Fan, Y. N. Gao, H. H. Wang, A. Robertson, S. Hong, Y. S. Jung, S. Z. Liu and Z. Y. Sun, Nitrogen Fixation by Ru Single-Atom Electrocatalytic Reduction, *Chem*, 2019, **5**, 204–214.

8 C. Lv, C. S. Yan, G. Chen, Y. Ding, J. X. Sun, Y. S. Zhou and G. H. Yu, An Amorphous Noble-Metal-Free Electrocatalyst that Enables Nitrogen Fixation under Ambient Conditions, *Angew. Chem., Int. Ed.*, 2018, **57**, 6073–6076.

9 G. N. Schrauzer and T. D. Guth, Photolysis of Water and Photoreduction of Nitrogen on Titanium Dioxide, *J. Am. Chem. Soc.*, 1977, **99**, 7189–7193.

10 A. Banerjee, B. D. Yuhas, E. Margulies, Y. B. Zhang, Y. Shim, M. Wasielewski and M. Kanatzidis, Photochemical Nitrogen Conversion to Ammonia in Ambient Conditions with FeMoS-Chalcogels, *J. Am. Chem. Soc.*, 2015, **137**, 2030–2034.

11 Y. X. Zhao, Y. F. Zhao, R. Shi, B. Wang, G. N. Waterhouse, L. Z. Wu, C. H. Tung and T. R. Zhang, Tuning Oxygen Vacancies in Ultrathin TiO2 Nanosheets to Boost Photocatalytic Nitrogen Fixation up to 700 nm, *Adv. Mater.*, 2019, **31**, 1806482.

12 Y. F. Zhao, Y. X. Zhao, G. Waterhouse, L. R. Zheng, X. Z. Cao, F. Teng, L. Z. Wu, C. H. Tung, D. O'Hare and T. R. Zhang, Layered-Double-Hydroxide Nanosheets as Efficient Visible-Light-Driven Photocatalysts for Dinitrogen Fixation, *Adv. Mater.*, 2017, **29**, 1703828.

13 P. S. Li, Z. Zhou, Q. Wang, M. Guo, S. W. Chen, J. X. Low, R. Long, W. Liu, P. R. Ding, Y. Y. Wu and Y. J. Xiong, Visible Light-Driven Nitrogen Fixation Catalyzed by Bi5O7Br Nanostructures: Enhanced Performance by Oxygen Vacancies, *J. Am. Chem. Soc.*, 2020, **142**, 12430–12439.

14 S. Zhang, Y. X. Zhao, R. Shi, C. Zhou, G. Waterhouse, Z. Wang, Y. X. Weng and T. R. Zhang, Sub-3 nm Ultrafine Cu2O for Visible Light Driven Nitrogen Fixation, *Angew. Chem.*, 2021, **133**, 2584–2590.

15 K. Ithisuphalap, H. G. Zhang, L. Guo, Q. G. Yang, H. P. Yang and G. Wu, Photocatalysis and Photoelectrocatalysis Methods of Nitrogen Reduction for Sustainable Ammonia Synthesis, *Small Methods*, 2019, **3**, 1800352.

16 X. Z. Chen, N. Li, Z. Z. Kong, W. J. Ong and X. J. Zhao, Photocatalytic Fixation of Nitrogen to Ammonia: State-of-the-art Advancements and Future Prospects, *Mater. Horiz.*, 2018, **5**, 9–27.

17 H. Li, J. Shang, Z. H. Ai and L. Z. Zhang, Efficient Visible Light Nitrogen Fixation with BiOBr Nanosheets of Oxygen Vacancies on the Exposed {001} Facets, *J. Am. Chem. Soc.*, 2015, **137**, 6393–6399.

18 M. Vu, M. Sakar and T. Do, Photo(electro)catalytic Nitrogen Fixation: Problems and Possibilities, *Adv. Mater. Interfaces*, 2019, **6**, 1900091.

19 Z. H. Wang, X. Hu, Z. Z. Liu, G. J. Zou, G. N. Wang and K. Zhang, Recent Developments in Polymeric Carbon Nitride-derived Photocatalysts and Electrocatalysts for Nitrogen Fixation, *ACS Catal.*, 2019, **9**, 10260–10278.

20 Y. Z. Guo, J. H. Yang, D. H. Wu, H. Y. Bai, Z. Yang, J. F. Wang and B. C. Yang, Au Nanoparticle-embedded, Nitrogen-deficient Hollow Mesoporous Carbon Nitride Spheres for Nitrogen Photofixation, *J. Mater. Chem. A*, 2020, **8**, 16218.

21 K. Brown, D. Harris, M. Wilker, A. Rasmussen, N. Khadka, H. Hamby, S. Keable and G. Dukovic, Light-driven Dinitrogen Reduction Catalyzed by a CdS:nitrogenase MoFe Protein Biohybrid, *Science*, 2016, **352**, 448–450.

22 B. Chica, J. Ruzicka, H. Kallas, D. Mulder, K. A. Brown, J. W. Peters, L. C. Seefeldt, G. Dukovic and P. King, Defining Intermediates of Nitrogenase MoFe Protein during N2 Reduction under Photochemical Electron Delivery from CdS Quantum Dots, *J. Am. Chem. Soc.*, 2020, **142**, 14324–14330.

23 J. Li, P. Liu, Y. Z. Tang, H. L. Huang, H. Z. Cui, D. H. Mei and C. L. Zhong, Single-Atom Pt-N3 Sites on the Stable Covalent Triazine Framework Nanosheets for Photocatalytic N2 Fixation, *ACS Catal.*, 2020, **10**, 2431–2442.

24 L. Li, Y. C. Wang, S. Vanka, X. Y. Mu, Z. T. Mi and C. J. Li, Nitrogen Photofixation over III-Nitride Nanowires Assisted by Ruthenium Clusters of Low Atomicity, *Angew. Chem., Int. Ed.*, 2017, **56**, 8701–8705.

25 H. M. Liu, P. Wu, H. T. Lia, Z. B. Chen, L. Z. Wang, X. Zeng, Y. X. Zhu, Y. J. Jiang, X. Z. Liao, J. H. Yee, C. Stampfl and J. Huang, Unravelling the Effects of Layered Supports on Ru Nanoparticles for Enhancing N2 Reduction in Photocatalytic Ammonia Synthesis, *Appl. Catal., B*, 2019, **259**, 118026.

26 N. Cao and G. F. Zheng, Aqueous Electrocatalytic N2 Reduction under Ambient Conditions, *Nano Res.*, 2018, **11**, 2992–3008.

27 X. L. Xue, R. P. Chen, C. Z. Yan, P. Y. Zhao, Y. Hu, W. J. Zhang, S. Y. Yang and Z. Jin, Review on Photocatalytic and Electrocatalytic Artificial Nitrogen Fixation for

Ammonia Synthesis at Mild Conditions: Advances, Challenges and Perspectives, *Nano Res.*, 2019, **12**, 1229–1249.

28 J. Zhang, X. Y. Tian, M. J. Liu, H. Guo, J. D. Zhou, Q. Y. Fang, Z. Liu, Q. Wu and J. Lou, Cobalt-Modulated Molybdenum–Dinitrogen Interaction in MoS2 for Catalyzing Ammonia Synthesis, *J. Am. Chem. Soc.*, 2019, **141**, 19269–19275.

29 H. Fei, T. Guo, Y. Xin, L. B. Wang, R. Q. Liu, D. Z. Wang, F. Y. Liu and Z. Z. Wu, Sulfur Vacancy Engineering of MoS2 via Phosphorus Incorporation for Improved Electrocatalytic N2 Reduction to NH3, *Appl. Catal., B*, 2022, **300**, 120733.

30 J. Zhang, X. Y. Tian, M. J. Liu, H. Guo, J. D. Zhou, Q. Y. Fang, Z. Liu, Q. Wu and J. Lou, Cobalt-Modulated Molybdenum-Dinitrogen Interaction in MoS2 for Catalyzing Ammonia Synthesis, *J. Am. Chem. Soc.*, 2019, **141**, 19269–19275.

31 X. S. Xu, B. T. Sun, Z. Q. Liang, H. Z. Cui and J. Tian, High-performance Electrocatalytic Conversion of N2 to NH3 Using 1T-MoS2 Anchored on Ti3C2 MXene under Ambient Conditions, *ACS Appl. Mater. Interfaces*, 2020, **12**, 26060–26067.

32 X. Liu, X. L. Han, Z. Q. Liang, Y. J. Xue, Y. L. Zhou, X. L. Zhang, H. Z. Cui and J. Tian, Phosphorous-doped 1T-MoS2 Decorated Nitrogen-doped g,-C3N4 Nanosheets for Enhanced Photocatalytic Nitrogen Fixation, *J. Colloid Interface Sci.*, 2022, **605**, 320–329.

33 N. Li, J. Liu, B. X. Dong and Y. Q. Lan, Polyoxometalate-Based Compounds for Photo- and Electrocatalytic Applications, *Angew. Chem., Int. Ed.*, 2020, **59**, 20779–20793.

34 M. Vasilopoulou, M. Douvas, C. Palilis, S. Kennou and P. Argitis, Old Metal Oxide Clusters in New Applications: Spontaneous Reduction of Keggin and Dawson Polyoxometalate Layers by a Metallic Electrode for Improving Efficiency in Organic Optoelectronics, *J. Am. Chem. Soc.*, 2015, **137**, 6844–6856.

35 X. X. Li, L. Zhang, J. Liu, L. Yuan, T. Wang, J. Y. Wang, L. Z. Dong, K. Huang and Y. Q. Lan, Design of Crystalline Reduction-Oxidation Cluster-Based Catalysts for Artificial Photosynthesis, *JACS Au*, 2021, **1**, 1288–1295.

36 X. C. Song, B. Li, W. C. Peng, C. Wang, K. Li, Y. Z. Zhu and Y. Mei, A Palladium Doped 1T-phase Molybdenum Disulfide-black Phosphorene Two-dimensional Van Der Waals Heterostructure for visible-light enhanced electrocatalytic hydrogen evolution, *Nanoscale*, 2021, **13**, 5892.

37 X. H. Zhang, N. Li, J. J. Wu, Y. Z. Zheng and X. Tao, Defect-rich O-incorporated 1T-MoS2 Nanosheets for Remarkably Enhanced Visible-light Photocatalytic H2 Evolution over CdS: The Impact of Enriched Defects, *Appl. Catal., B*, 2018, **229**, 227–236.

38 W. J. Ong, L. L. Tan, S. P. Chai, S. T. Yong and A. Mohamed, Surface Charge Modification via Protonation of Graphitic Carbon Nitride (g-C3N4) for Electrostatic Self-assembly Construction of 2D/2D Reduced Graphene Oxide (rGO)/g,-C3N4 Nanostructures toward Enhanced Photocatalytic Reduction of Carbon Dioxide to Methane, *Nano Energy*, 2015, **13**, 757–770.

39 Z. Q. Liang, Y. J. Xue, Y. C. Guo, G. S. Zhang, H. Z. Cui and J. Tian, Rationalizing and Controlling the Phase Transformation of Semi-metallic 1T'-phase and Semi-conductive 2H-phase MoS2 as Cocatalysts for Photocatalytic Hydrogen Evolution, *Chem. Eng. J.*, 2020, **396**, 125344.

40 V. Nguyen, A. Mady, M. Mahadadalkar, M. Baynosa, D. Kumar, A. Rabie, J. Lee, W. Kim and J. Shim, Highly Active Z-scheme Heterojunction Photocatalyst of Anatase TiO2 Octahedra Covered with C-MoS2 Nanosheets for Efficient Degradation of Organic Pollutants under Solar Light, *J. Colloid Interface Sci.*, 2022, **606**, 337–352.

41 W. Kim, G. B. Yuan, A. McClure and H. Frei, Light Induced Carbon Dioxide Reduction by Water at Binuclear ZrOCoII Unit Coupled to Ir Oxide Nanocluster Catalyst, *J. Am. Chem. Soc.*, 2014, **136**, 11034–11042.

42 L. Li, Z. D. Qin, L. Ries, S. Hong, T. Michel, J. Yang, C. Salameh, M. Bechelany, P. Miele, D. Kaplan, M. Chhowalla and D. Voiry, Role of Sulfur Vacancies and Undercoordinated Mo Regions in MoS2 Nanosheets toward the Evolution of Hydrogen, *ACS Nano*, 2019, **13**, 6824–6834.

43 L. Cai, J. F. He, Q. H. Liu, T. Yao, L. Chen, W. S. Yan, F. C. Hu, Y. Jiang, Y. D. Zhao, T. D. Hu, Z. H. Sun and S. Q. Wei, Vacancy-Induced Ferromagnetism of MoS2 Nanosheets, *J. Am. Chem. Soc.*, 2015, **137**, 2622–2627.

44 K. Chang, X. Hai, H. Pang, H. B. Zhang, L. Shi, G. G. Liu, H. M. Liu, G. X. Zhao, M. Li and J. H. Ye, Targeted Synthesis of 2H- and 1T-Phase MoS2 Monolayers for Catalytic Hydrogen Evolution, *Adv. Mater.*, 2016, **28**, 10033–10041.

45 N. Luo, C. Chen, D. M. Yang, W. Y. Hua and F. Q. Dong, S defect-rich ultrathin 2D MoS2: The Role of S Point-defects and S Stripping-defects in the Removal of Cr(VI) via Synergistic Adsorption and Photocatalysis, *Appl. Catal., B*, 2021, **299**, 120664.

46 J. Zhou, J. Zhao and R. Liu, Defect Engineering of Zeolite Imidazole Framework Derived ZnS Nanosheets towards Enhanced Visible Light Driven Photocatalytic Hydrogen Production, *Appl. Catal., B*, 2020, **278**, 119265.

47 X. Liu, Y. X. Zhao, X. F. Yang, Q. Q. Liu, X. H. Yua, Y. Y. Lid, H. Tang and T. R. Zhang, Porous Ni5P4 as a Promising Cocatalyst for Boosting the Photocatalytic Hydrogen Evolution Reaction Performance, *Appl. Catal., B*, 2020, **275**, 119144.

48 T. Wang, M. Xu, C. H. Ma, Y. T. Gu, W. C. Chen, J. Gong, T. Ji and W. L. Chen, Strategic Design of a Bifunctional NiFeCoW@NC Hybrid to Replace the Noble Platinum for Dye-Sensitized Solar Cells and Hydrogen Evolution Reactions, *ACS Appl. Mater. Interfaces*, 2021, **13**, 25010–25023.

49 X. Chang, X. F. Yang, Y. Qiao, S. Wang, M. H. Zhang, J. Xu, D. H. Wang and X. H. Bu, Confined Heteropoly Blues in Defected Zr-MOF (Bottle Around Ship) for High-Efficiency Oxidative Desulfurization, *Small*, 2020, **16**, 1906432.

50 D. Liu, B. K. Chen, J. Li, Z. G. Lin, P. H. Li, N. Zhen, Y. N. Chi and C. W. Hu, Imidazole-Functionalized Polyoxometalate Catalysts for the Oxidation of 5-Hydroxymethylfurfural to 2,5-Diformylfuran Using Atmospheric O2, *Inorg. Chem.*, 2021, **60**, 3909–3916.

51 X. T. Li, X. D. Lv, N. Li, J. J. Wu, Y. Z. Zheng and X. Tao, One-step Hydrothermal Synthesis of High-percentage 1T-phase MoS2 Quantum Dots for Remarkably Enhanced Visible-light-driven Photocatalytic H2 Evolution, *Appl. Catal., B*, 2019, **243**, 76–85.

52 L. J. Shen, M. B. Luo, Y. H. Liu, R. W. Liang, F. F. Jing and L. Wu, Noble-metal-free MoS2 co-catalyst decorated UiO-66/CdS hybrids for efficient photocatalytic H2 production, *Appl. Catal., B*, 2015, **166–167**, 445–453.

53 H. L. Jia, A. Du, H. Zhang, J. H. Yang, R. B. Jiang, J. F. Wang and C. Y. Zhang, Site-Selective Growth of Crystalline Ceria with Oxygen Vacancies on Gold Nanocrystals for Near-Infrared Nitrogen Photofixation, *J. Am. Chem. Soc.*, 2019, **141**, 5083–5086.

54 C. Y. Hu, X. Chen, J. B. Jin, Y. Han, S. M. Chen, H. X. Ju, J. Cai, Y. R. Qiu, C. Gao, C. M. Wang, Z. M. Qi, R. Long, L. Song, Z. Liu and Y. J. Xiong, Surface Plasmon Enabling Nitrogen Fixation in Pure Water through a Dissociative Mechanism under Mild Conditions, *J. Am. Chem. Soc.*, 2019, **141**, 7807–7814.

55 J. H. Yang, H. Y. Bai, Y. Z. Guo, H. Zhang, R. B. Jiang, B. C. Yang, J. F. Wang and J. Yu, Photodriven Disproportionation of Nitrogen and Its Change to Reductive Nitrogen Photofixation, *Angew. Chem.*, 2021, **133**, 940–949.

56 N. Zhang, A. Jalil, D. X. Wu, S. M. Chen, Y. F. Liu, C. Gao, W. Ye, Z. M. Qi, H. X. Ju, C. M. Wang, X. J. Wu, L. Song, J. F. Zhu and Y. J. Xiong, Refining Defect States in W18O49 by Mo Doping: A Strategy for Tuning N2 Activation towards Solar-Driven Nitrogen Fixation, *J. Am. Chem. Soc.*, 2018, **140**, 9434–9443.

57 T. T. Hou, R. H. Guo, L. L. Chen, J. S. Guo, W. H. Zhang, X. S. Zheng, W. K. Zhu, X. P. Tan and L. B. Wang, Atomic-level insights in tuning defective structures for nitrogen photofixation over amorphous SmOCl nanosheets, *Nano Energy*, 2019, **65**, 104003.

58 Q. D. Yue, Y. Y. Wan, Z. J. Sun, X. J. Wu, Y. P. Yuan and P. W. Du, MoP is a Novel, Noble-metal-free Cocatalyst for Enhanced Photocatalytic Hydrogen Production from Water under Visible Light, *J. Mater. Chem. A*, 2015, **3**, 16941.

